Dynamical analysis of galaxy cluster merger Abell 2146

J. A. White,[1,2]* R. E. A. Canning,[3,4] L. J. King,[1] B. E. Lee,[1] H. R. Russell,[5]
S. A. Baum,[6,7] D. I. Clowe,[8] J. E. Coleman,[1] M. Donahue,[9] A. C. Edge,[10]
A. C. Fabian,[5] R. M. Johnstone,[5] B. R. McNamara,[11] C. P. O'Dea[6,7]
and J. S. Sanders[12]

[1]*Department of Physics, University of Texas at Dallas, 800 W. Campbell Road, Richardson, TX 75080, USA*
[2]*Physics and Astronomy Department, University of British Columbia, 6224 Agricultural Road, Vancouver, BC V6T 1Z1, Canada*
[3]*Kavli Institute for Particle Astrophysics and Cosmology (KIPAC), Stanford University, 452 Lomita Mall, Stanford, CA 94305-4085, USA*
[4]*Department of Physics, Stanford University, 452 Lomita Mall, Stanford, CA 94305-4085, USA*
[5]*Institute of Astronomy, University of Cambridge, Madingley Road, Cambridge CB3 0HA, UK*
[6]*School of Physics & Astronomy, Rochester Institute of Technology, Rochester, NY 14623, USA*
[7]*Department of Physics & Astronomy, University of Manitoba, Winnipeg, MB R3T 2N2, Canada*
[8]*Department of Physics and Astronomy, Ohio University, 251B Clippinger Lab, Athens, OH 45701, USA*
[9]*Department of Physics & Astronomy, Michigan State University, 567 Wilson Rd, East Lansing, MI 48824, USA*
[10]*Department of Physics, Durham University, Durham DH1 3LE, UK*
[11]*Department of Physics & Astronomy, University of Waterloo, N2L 3G1 Waterloo, Canada*
[12]*Max-Planck-Institut für extraterrestrische Physik, Giessenbachstrasse 1, D-85748 Garching, Germany*

ABSTRACT

We present a dynamical analysis of the merging galaxy cluster system Abell 2146 using spectroscopy obtained with the Gemini Multi-Object Spectrograph on the Gemini North telescope. As revealed by the *Chandra* X-ray Observatory, the system is undergoing a major merger and has a gas structure indicative of a recent first core passage. The system presents two large shock fronts, making it unique amongst these rare systems. The hot gas structure indicates that the merger axis must be close to the plane of the sky and that the two merging clusters are relatively close in mass, from the observation of two shock fronts. Using 63 spectroscopically determined cluster members, we apply various statistical tests to establish the presence of two distinct massive structures. With the caveat that the system has recently undergone a major merger, the virial mass estimate is $M_{\rm vir} = 8.5^{+4.3}_{-4.7} \times 10^{14}\,{\rm M_\odot}$ for the whole system, consistent with the mass determination in a previous study using the Sunyaev–Zel'dovich signal. The newly calculated redshift for the system is $z = 0.2323$. A two-body dynamical model gives an angle of $13°–19°$ between the merger axis and the plane of the sky, and a time-scale after first core passage of $\approx 0.24–0.28$ Gyr.

Key words: galaxies: clusters: general – galaxies: clusters: individual: A2146.

1 INTRODUCTION

Galaxy clusters are formed hierarchically through the mergers of smaller clusters and groups. Mergers of galaxy clusters are the most energetic events since the big bang, with a total kinetic energy that can reach 10^{57} J (e.g. Sarazin 2001), and major mergers close to the plane of the sky are very rare systems but of extreme importance in cosmology (e.g. Clowe et al. 2006; Markevitch & Vikhlinin 2007). Most of the mass in galaxy clusters is dark matter, and the bulk of baryonic mass is in the form of ionized plasma, comprising about 15 per cent of the total mass. During a merger, as the plasma clouds of each cluster pass through each other they are affected by ram pressure, causing them to slow down. The galaxies in a cluster are effectively collisionless and are affected primarily by tidal interactions during the merger. Dark matter does not have a large cross-section for self-interaction (e.g. Markevitch et al. 2004; Randall et al. 2008), so shortly after collision the plasma clouds are expected to lag behind the dark matter and the major concentrations of cluster galaxies (e.g. Clowe et al. 2006). A merger thus results in an offset between the dominant luminous component, imaged using X-ray telescopes, and the total mass, mapped using gravitational lensing.

Abell 2146 is in the throes of a major merger (Russell et al. 2010) and X-ray maps show a structure similar to the 'Bullet cluster' (Markevitch et al. 2002; Clowe et al. 2006). Unique among merger
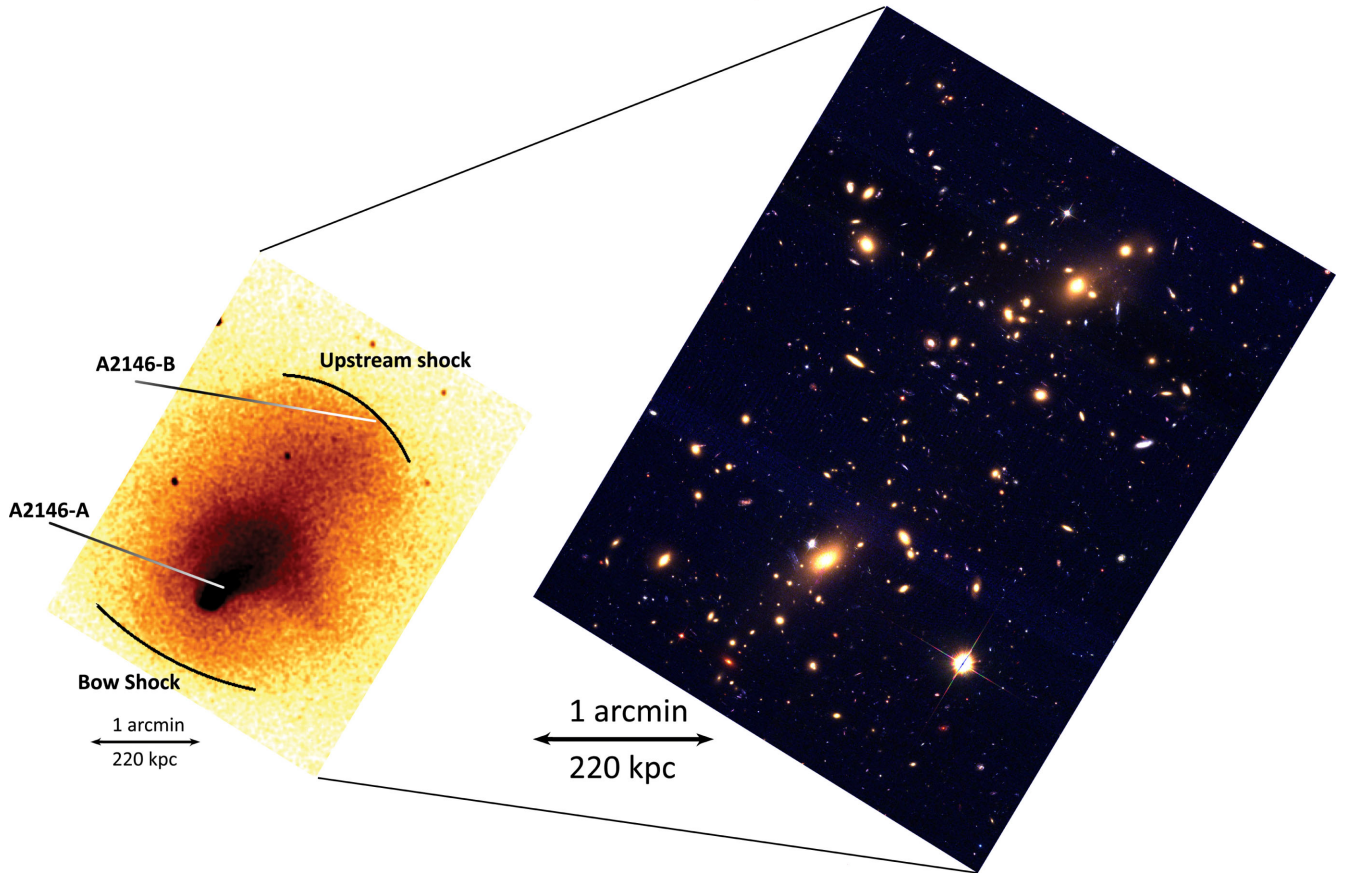
Figure 1. Left: exposure-corrected Chandra X-ray image for the 0.3–7 keV energy band (north is up and east is to the left). The image has been smoothed with a 2D Gaussian of width 1.5 arcsec. Right: *HST F*435*W*, *F*606*W*, *F*814*W*, colour composite image of Abell 2146.

systems, two clear shock fronts are detected in the *Chandra* X-ray temperature and density maps indicating Mach numbers of ≈2.3 for the bow shock and ≈1.6 for the upstream shock, and corresponding velocities in the plane of the sky of 2700^{+400}_{-300} km s^{-1} and 2400 ± 300 km s^{-1}, respectively (Russell et al. 2012). From the shock velocity and the projected distance from the collision site, Russell et al. (2010) estimate that the merger is observed 0.1–0.2 Gyr after core passage. The detection of the shock fronts is fully consistent with the merger being observed soon after first core passage (e.g. Sarazin 2001), but the time-scale is approximate due to uncertainty in the velocity of the subcluster – likely to be significantly lower than the shock velocity (e.g. Milosavljević et al. 2007; Springel & Farrar 2007) – and since the location of the collision site is not precisely known.

In Fig. 1, we show the *Chandra* X-ray observatory image from Russell et al. (2012) and *Hubble Space Telescope* (*HST*) optical colour composite of Abell 2146 (Program 12871, PI King). Subclusters A and B are labelled on the left, with subcluster A being located at the head of the 'bullet' in the south-east. The brightest cluster galaxy (hereafter BCG) of the SE subcluster (A2146-A), is in an unexpected location lagging *behind* the X-ray cool core (Canning et al. 2012). As noted above, in the early stages of a cluster merger the galaxies should be nearly collisionless and follow the dark matter distribution, which should lead the collisional X-ray gas (e.g. Markevitch & Vikhlinin 2001; Clowe et al. 2006).

In addition to the strange projected location of the BCG in Abell 2146-A, the system is unusual in that despite it appearing to undergo a major galaxy cluster merger it does not have a detected radio halo (Russell et al. 2011). Studies of samples of radio haloes in clusters have shown that they are found almost exclusively in morphologically disturbed clusters, indicating that their generation is associated with acceleration or re-acceleration of energetic particles in the highly shocked cluster gas, and that there is a relationship between the radio power of the halo, P_{radio}, and the X-ray luminosity of the cluster, L_X (Giovannini & Feretti 2000; Liang et al. 2000; Buote 2001; Brunetti et al. 2009; Cassano et al. 2010; Rossetti et al. 2011). The conditions under which radio haloes are generated in clusters, such as the cluster masses, velocities and time-scales, are still open questions. Merging clusters, such as Abell 2146, which do not exhibit these features may be a powerful diagnostic to test models of radio halo generation.

In this paper we present multi-object spectroscopy of the system, in order to identify substructure and to provide a complementary method of probing the dynamical status, time-scale of the merger, and mass of the system (e.g. Girardi et al. 1998; Barrena et al. 2002; Ferrari et al. 2005). Section 2 will briefly describe the optical sample selection, and observations and data reduction will be the subject of Section 3. Results from an analysis of the substructure within the Abell 2146 system will be presented in Section 4, and Section 5 will discuss these results in the context of simple dynamical models. Section 6 presents a summary and discussion of our results. A future paper will address the stellar populations of the system.

Throughout this paper, we assume a ΛCDM cosmology with present day Hubble parameter $H_0 = 70$ km s^{-1} Mpc^{-1}, matter density parameter $\Omega_m = 0.3$, and dark energy density parameter $\Omega_\Lambda = 0.7$ (we assume a cosmological constant, equation of state
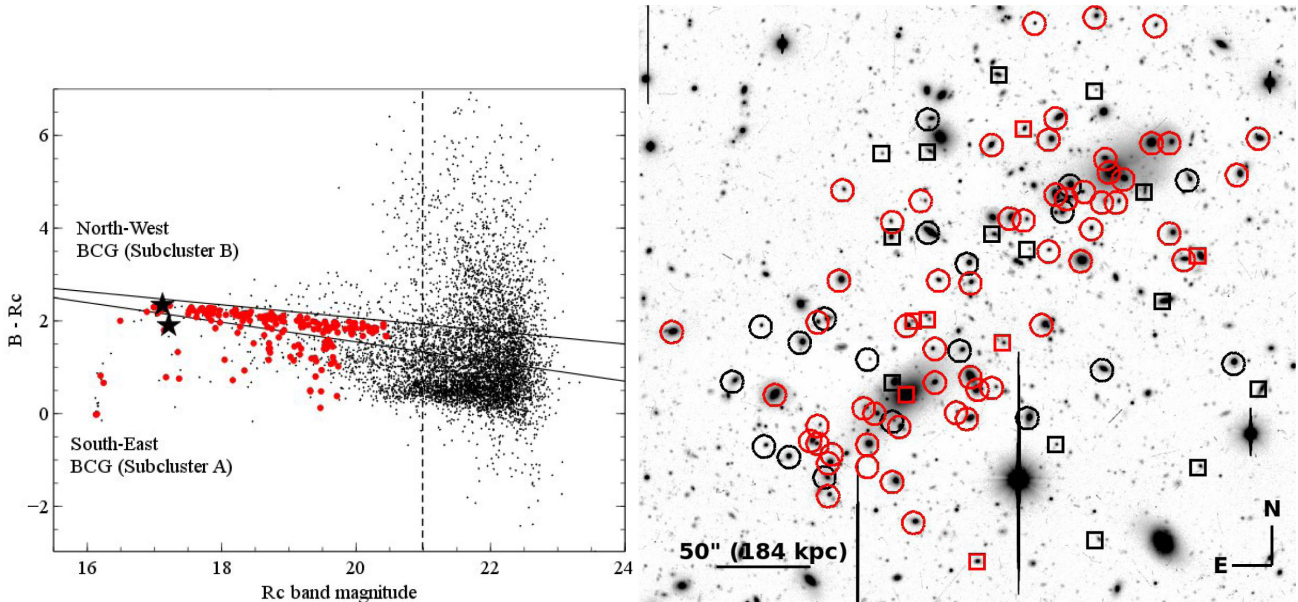
Figure 2. Target selection for GMOS spectroscopy: targets were chosen based on colour, magnitude and cluster-centric distance, detected from our *Subaru* Suprime-Cam imaging. Left: colour–magnitude diagram for galaxies within 3 arcmin of the centre of the system. The dashed line indicates the initial apparent magnitude cut which we imposed on our sample. The red sequence was determined by fitting a Gaussian in magnitude bins of $18 > Rc$, $18 < Rc < 19.5$, $19.5 < Rc < 21$ and $21 < Rc$. The final 170 galaxies selected from our catalogue by the GEMINI mask making tools are indicated in red and the two BCGs are marked by black stars. Right: the 97 objects for which we determined redshifts overlaid on our *Subaru* Suprime-Cam composite colour image; those found to be cluster members are indicated in red and those not in the cluster indicated in white. The circles in each case indicate galaxies which fall on the red sequence, while the boxes indicate galaxies bluewards of the red sequence.

parameter $w = -1$). For this cosmology and at the redshift of Abell 2146 ($z = 0.2323$), an angular size of 1 arcsec corresponds to a physical scale of ≈ 3.677 kpc.

2 OPTICAL SAMPLE SELECTION

Here, we briefly present the criteria for selecting the galaxy sample for GEMINI GMOS-N multi-object spectrograph (MOS) observations of Abell 2146. The next section will outline the observations and data reduction.

Targets were detected on our Rc band optical *Subaru* imaging using SEXTRACTOR (Bertin & Arnouts 1996). We restricted our target galaxies to those brighter than 21 apparent magnitude and to those within 3 arcmin from the centre of the Abell 2146 system. We then determined the cluster 'red-sequence' by binning the galaxies into magnitude bins of $18 > Rc$, $18 < Rc < 19.5$, $19.5 < Rc < 21$ and $21 < Rc$ mags. We fit two Gaussians to the bimodal population of colour in each magnitude bin; one defining the 'red sequence' and one defining the 'blue cloud', and took the 3σ boundaries of the Gaussian defining the red sequence to determine its width in each magnitude bin. We then fit a linear relation to the red sequence (black solid lines in Fig. 2). We identify 337 targets with $Rc < 21$ mags on the cluster red sequence (see Fig. 2, left).

Many galaxies morphologically associated with the X-ray shock fronts and one of the BCGs do not lie on the red sequence. For this reason, we additionally add 50 targets to our target list (including 12 acquisition targets) based on an inspection of the *Subaru* images. In particular, we added the south-east BCG and targets close to the BCGs and X-ray shock front which were too blue to be included on the red sequence. We also added two possible strong lensing features to our target list. Finally, we have a sample of 375 target objects and a further 12 acquisition objects to input to the Gemini MOS Mask Preparation Software (GMMPS).

The two BCGs, galaxies close to the shock front and strong lensing features were assigned the highest priority. All other targets were prioritized by magnitude then cluster-centric distance and the GMMPS was iteratively run in order to fit as many objects as possible on the masks while requiring at least three acquisition objects per mask. Finally, we obtained seven masks totalling spectra on 170 targets indicated by red points on the left-hand panel of Fig. 2. Of the 170 targets observed with GEMINI 139 lie on the red sequence giving a red sequence completeness of 67 per cent at $Rc < 20.5$ mags within 3 arcmin of the centre of the Abell 2146 system. As described in Section 3, we were able to obtain redshifts for 97 galaxies, of which 63 were determined to be cluster members and are tabulated in the appendix (see appendix and Section 4). The 97 objects are indicated on the right-hand panel of Fig. 2 with the cluster members in red. Objects indicated by circles are those determined to be on the red sequence, while those indicated by boxes are found bluewards of the red sequence.

3 OBSERVATIONS AND DATA REDUCTION

Spectroscopic observations of Abell 2146 were carried out with the Gemini Multi-object Spectrograph (GMOS) at the Gemini North Telescope on Mauna Kea, Hawaii. They were made over the course of four nights between 2012 April 19 and May 1 (Program ID: GN-2012A-Q-47, PI Canning). We used the GMOS-MOS instrument equipped with the B600+_G5307 grating. This configuration yielded a dispersion of 0.50 Å pixel^{-1}. The 5.5 arcmin field of view of the GMOS detector allowed observations to be made in a single pointing.

Using slit widths of 1 arcsec and slit lengths of 5 arcsec, between 18 and 31 objects were able to be targeted in each mask. Due to the densely packed nature of the field, seven masks were used to obtain spectra of a total of 170 science targets. Three 1200 s exposures were
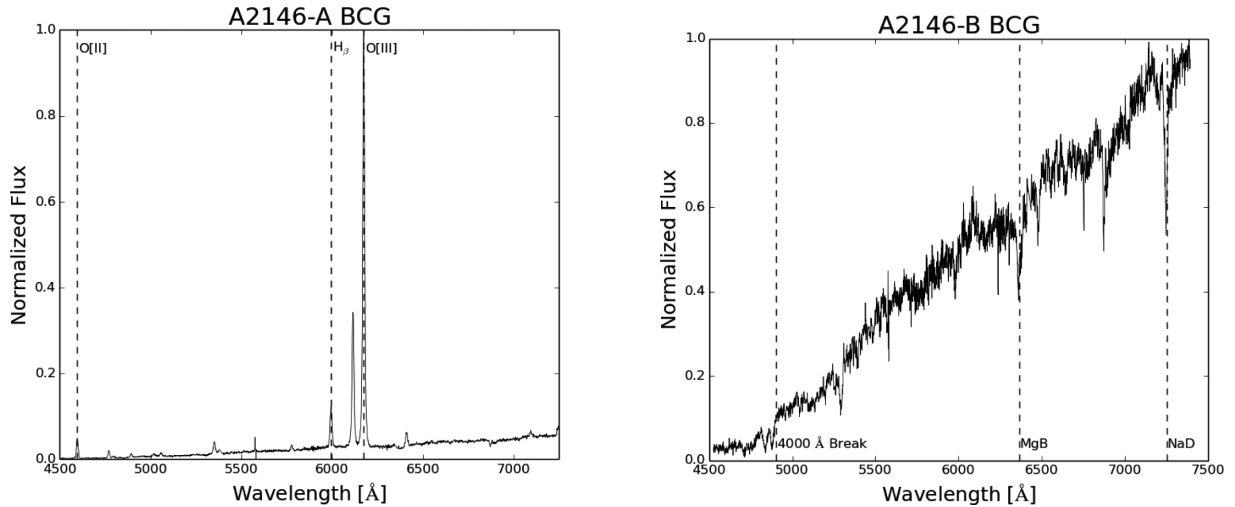
Figure 3. One-dimensional extracted spectra of the BCGs in A2146-A (left) and A2146-B (right). Spectra are shown at the observed wavelengths. Various emission and absorption features are labelled.

taken with each mask in order to achieve an S/N ~ 3 per spectral pixel, at the redshift of the 4000 Å break for the faintest galaxies in our target list (determined using GEMINI GMOS exposure time calculator). Wavelength calibration was performed using Helium–Argon lamps.

The data reduction was performed using the Gemini package in IRAF;[1] see Fig. 3 for examples of the resulting spectra. All science exposures, comparison lamps, and flats were overscan/bias subtracted and trimmed. The resulting reduced spectra were then processed to remove cosmic rays, wavelength calibrated, extracted to 1D and combined.

The cross-correlation method was used to calculate radial velocities through the RVSAO[2] package in IRAF. A catalogue of 23 different templates from the RVSAO library (Kurtz & Mink 1998), including stars, quasars, and emission and absorption line galaxy template spectra was used to determine the radial velocities. In order to determine the templates to use in the final analysis, we relied on a combination of visual examination and the R value returned by RVSAO. Each extracted 1D target spectrum was visually examined and a redshift identified by at least two members of the team, with a third examining spectra where disagreements were found. For 54/170 objects no redshift was able to be determined with a visual inspection due to a low signal to noise (S/N). For a further 19/170 targets, the visual examinations yielded a redshift which was not consistent with the radial velocity measurements for any of the 23 RVSAO template spectra. In both these cases, the targets were not used in the remainder of the analysis in this paper. In 73/170 targets, the visual examination yielded a redshift within ± 6000 km s^{-1} of the RVSAO radial velocity with the highest R value. In these cases the radial velocity corresponding to the highest R-value template was used. In the remainder (24/170), the highest R-value template did not correspond to the visually determined cz. However, a template with R value smaller than the best value did have a radial velocity within ± 5000 km s^{-1} of the visual

velocity. If $\Delta R < 5$ then we accepted the fit with a lower R after further examination of the template spectra. In most of these 24 targets poor sky subtraction was the reason for poor template fitting. However, the *HST* imaging has shown many lensed features are apparent in the Abell 2146 system and galaxy density is high. Some poor redshifts may be due to blending between two of more sources. The spectra of the BCGs in A2146-A and A2146-B are shown in Fig. 3.

In order to minimize errors associated with cross-correlation and to correct for artefacts in the spectra (such as cosmic rays), three separate observations of each object were made and then the spectra were co-added together (e.g. Gallazzi et al. 2008). This signal averaging helps to increase the S/N of the spectrum and can help to remove certain undesirable features that are only contained in one of the individual spectra. The radial velocities and errors were then compared to both the co-added and individual spectra.

4 A2146 STRUCTURE

4.1 Cluster member determination

The target radial velocities were used to determine cluster membership: first, we made a $\pm 10\,000$ km s^{-1} cut at the previously calculated cluster redshift of $z = 0.2343$ (Struble & Rood 1999), as was done by Ferrari et al. (2005). Cluster members were then determined by a 2.5σ clip of the remaining objects. This leaves a total of 63 galaxies out of the 97 objects for which we could determine a redshift. Fig. 2 shows the 63 objects identified as cluster members circled in red. The foreground and background objects are identified in white. The velocity distribution for the 97 targets (which are not stars) is shown in the top panel of Fig. 4, while the bottom panel shows only the 63 cluster members after σ clipping.

4.2 Subclustering

The velocity distribution of the Abell 2146 system is shown in Fig. 4. We apply a Lilliefors test to determine whether the velocity distribution of the 63 cluster member galaxies is statistically different from a Gaussian distribution. We calculate a p-value of 0.23

[1] IRAF is distributed by the National Optical Astronomy Observatories, which are operated by the Association of Universities for Research in Astronomy, Inc., under cooperative agreement with the National Science Foundation.
[2] RVSAO was developed at the Smithsonian Astrophysical Observatory Telescope Data Center.
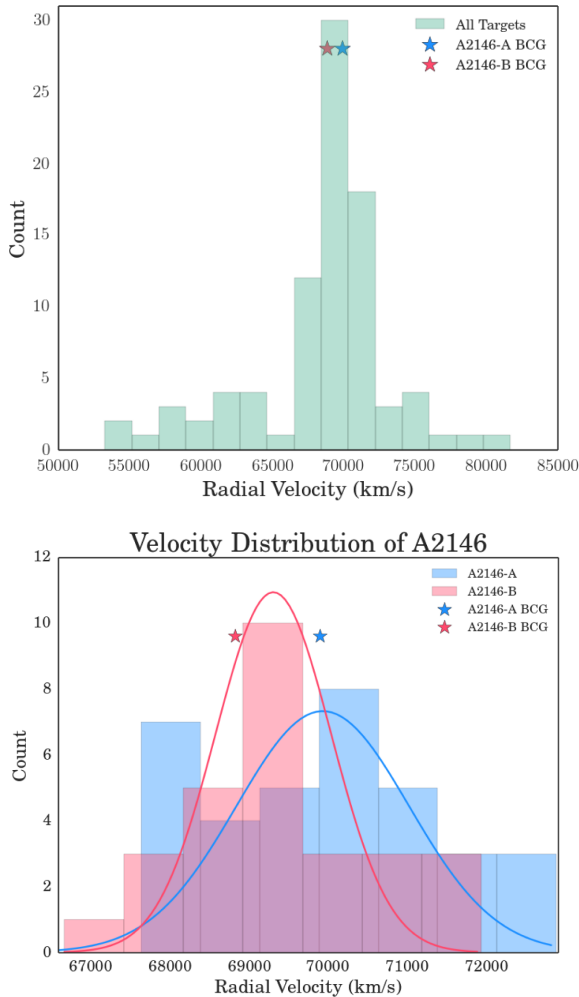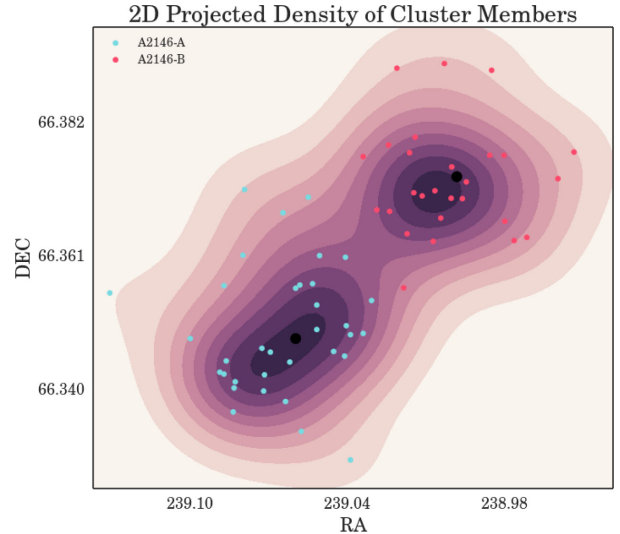
Figure 5. Projected density map of cluster members in 2D. The relative density contour map is shown in position space. The subcluster A2146-A is on the bottom left (blue circles) and A2146-B (red circles) is on the top right with the BCGs in both subclusters represented with a black point. In the figure north is up and east is to the left.

Figure 4. Top: the radial velocity histogram for all objects where a reliable redshift was determined and the targets are not stars. The cluster radial velocities peak around 70 000 km s^{-1}, however, there is no evidence in our data that the broad tails in the distribution correspond to further clustering of galaxies. Bottom: radial velocity distribution of cluster members. Cluster members in A2146-A are shown in blue, and A2146-B in red. The solid lines indicate a Gaussian profile at the biweight mean. The radial velocities of the two BCGs are denoted by stars. Subcluster membership was determined using the KMM algorithm (Ashman, Bird & Zepf 1994).

indicating that the null hypothesis, that the velocity distribution of the system as a whole is Gaussian distributed, cannot be rejected. However, for a plane of sky merger this is not a sufficient condition to exclude the presence of subclustering.

To investigate the possibility of subclustering further, we apply the Dressler–Schectman test (Dressler & Shectman 1988, henceforth DS test) and also carry out an analysis of the 2D projected density of cluster members.

First, we apply the DS test which provides a useful statistic to determine the likelihood of subclustering. The DS test compares the kinematics of a sample of size $N_{\rm nn}$ to the kinematics of the whole system. For each galaxy in the field, the distances are computed between every pair in the system and then the $N_{\rm nn}$ nearest neighbours are chosen for analysis. The statistic is given by

$$\delta_i^2 = \frac{N_{\rm nn}}{\sigma_v^2}[(\bar{v}_{\rm local} - \bar{v})^2 + (\sigma_{\rm local} - \sigma_v)^2], \qquad (1)$$

where σ_v is the velocity dispersion of the whole group and $\sigma_{\rm local}$ is the velocity dispersion of the ith sample. These values are summed to obtain

$$\Delta = \sum_i^N \delta_i, \qquad (2)$$

with $\frac{\Delta}{N} > 1$ being an indicator of substructure present in the field. Using $N_{\rm nn} = \sqrt{N_{\rm Total}}$ we found a $\frac{\Delta}{N} = 1.08$. The marginal result makes it hard to determine if there is substructure in the system (see also Pinkney et al. 1996 for the results of applying the DS test to simulated galaxy clusters).

To test if the calculated Δ was significantly different from random, we randomly shuffled the velocities of the objects while holding the positions fixed. Repeating this process 10 000 times, we found that the fraction of random velocities that gave a larger Δ was $P = 0.18$, where a value of P less than 0.1 would be expected for a non-random distribution. Thus, we conclude that the DS test results are not strong enough to indicate substructure in the system. We return to this result in the Discussion.

Secondly, we analyse the 2D projected density of all of the cluster members. Cluster members identified by their redshift were plotted in RA and DEC space with overlaying contours determined using a Kernel Density Estimator (KDE) and a Gaussian kernel. The KDE utilized a Silverman bandwidth. Since Gaussian kernels are less sensitive to bimodal distributions, this test will be biased towards strong substructure detections. The results plotted in Fig. 5 clearly show that two density peaks are present in the data. This confirms the existence of at least two subclusters and is consistent with the *Chandra* X-ray data which shows a bi-model merger morphology with both forward and reverse shocks detected in the X-ray analysis and along the same axis as our two subcluster clumps (Russell et al. 2012). The KDE analysis allows us to conclude that there is substructure present in the system.

Having confirmed the presence of substructure, we wish to identify the cluster members of particular subclusters in order to characterize properties such as the mass of the substructures, the time-scale since core passage of the merger and the presence of any offsets

between the galaxy and hot gas populations. In order to assign the cluster members to particular subclusters we apply the KMM algorithm (Ashman et al. 1994). This determines the mixture of multi-dimensional Gaussians which are best fit to a set of data and the probability of each data point belonging to each Gaussian.

The clear X-ray shock fronts and the small line-of-sight velocity offsets of the two BCGs indicates strongly that our merger is likely to be in the plane of the sky. As such, the distribution of velocities from each subcluster is expected to have a significant overlap (as seen in Fig. 4). Including such similar velocity information in the KMM algorithm can lead to non-physical results in distinguishing between the two subcluster components. The analysis was carried out with position data only and yielded results which correspond well with the projected galaxy density peaks seen in Fig. 5. The KMM algorithm classified 35 galaxies as belonging to A2146-A and 28 belonging to A2146-B. These subcluster members are marked in Fig. 5 (with blue corresponding to A2146-A and red corresponding to A2146-B), and subcluster membership is also noted in Table A1 in the appendix. The velocity distribution of the galaxies identified in the two subclusters is shown in Fig. 4. The KMM algorithm is sensitive to outliers (Ashman et al. 1994) which is of particular importance for a cluster sample such as ours where the data are incomplete. We therefore bootstrap the sample (e.g. Waters et al. 2009) and re-run the KMM test 5000 times to determine which galaxies to assign to which subcluster and the centroid of our two subclusters. The centroids and their 68 per cent uncertainties are $239.062^{+0.004}_{-0.004}$, $66.349^{+0.002}_{-0.002}$ (15:56:14.9$^{+0.9}_{-0.9}$, 66:20:56.4$^{+7.2}_{-7.2}$) and $239.005^{+0.005}_{-0.005}$, $66.373^{+0.002}_{-0.002}$ (15:56:1.2$^{+1.2}_{-1.2}$, 66:22:22.8$^{+7.2}_{-7.2}$) for subclusters A and B, respectively.

Applying a Lilliefors test again to the individual subclusters yields a *p*-value of 0.83 for A2146-A and a *p*-value of 0.059 for A2146-B. This indicates that the velocity distribution for A2146-A can be adequately described by a Gaussian distribution. A Gaussian distribution for the velocities of subcluster A2146-B would be rejected at the 94 ($<2\sigma$) per cent level. There is evidence from a weak gravitational lensing mass reconstruction of *HST* data that A2146-B is rather more extended that A2146-A, possibly due to an intrinsically more elongated mass distribution (King L. J., in preparation). The number of galaxies for which we have spectroscopic data is insufficient to decide between these possibilities.

4.3 Velocity dispersions of the subclusters

The biweight estimator (Beers, Flynn & Gebhardt 1990) was applied to the cluster members for location and scale giving a mean apparent cluster redshift of $z = 0.2323$ (radial velocity of 69 640 km s^{-1}). The velocity dispersions were calculated from the median absolute deviation (MAD) (e.g. Ferrari et al. 2005) with errors estimated through a bootstrap technique. The velocity dispersions of the two subclusters are 1130^{+120}_{-320} km s^{-1} for the A2146-A subcluster and 760^{+360}_{-340} km s^{-1} for the A2146-B subcluster, with a 68 per cent confidence interval (CI). It is important to note that the distribution of radial velocities is undersampled and given that A2146 has recently undergone a merger, the distributions are possibly non-Gaussian. So the calculated velocity dispersions characterize the distribution, with the caveat that the sample may be non-Gaussian.

Application of the biweight estimator and bootstrap error approximations were carried out using the astropy library in the PYTHON programming language.[3] In a bootstrap technique, a 68 per cent

---

[3] http://docs.astropy.org/en/stable/

CI is found for the MAD. This approach draws many samples with replacement from the data available, estimates the MAD from each sample, then rank orders the means to estimate the 16 and 84 percentile values for 68 per cent CI. Unlike assuming normal distributions to calculate 68 per cent CI, the results calculated from the bootstrap are robust and can compensate for a data distribution that is far from normal.

The velocity distribution of cluster members is shown in the histogram in Fig. 4. The cluster members in A2146-A are shown in blue, and the cluster members in A2146-B are shown in red. Gaussian profiles for each subcluster are overlaid and centred at the mean determined from a biweight estimator (Beers et al. 1990).

5 A2146 DYNAMICS

5.1 Virial mass

A common way to estimate the mass of a galaxy cluster is through the virial theorem, which assumes dynamical stability (e.g. Araya-Melo, Van De Weygaert & Jones 2009), and therefore relates the time averaged kinetic energy to the potential energy as

$$\langle T \rangle = -\frac{1}{2} \sum_{i}^{N} V_i \, . \tag{3}$$

We calculate the virial masses below and tabulate them in Table 1, along with the Sunyaev–Zel'dovich (SZ) and X-ray derived masses from the literature (see Section 6). However, we caution that the Abell 2146 system is not dynamically relaxed and discuss the potential biases of the mass measurements in Section 6. The virial theorem relates the gravitational potential energy to the kinetic energy (relative velocities) of the cluster members and the mass is calculated via the following relation

$$M_{\mathrm{vir}} = \frac{3\pi}{G} \frac{\sigma_v^2}{R_{\mathrm{H}}}, \tag{4}$$

where σ_v is the velocity dispersion calculated in Section 4.3. R_{H} is the mean harmonic radius given by

$$\frac{1}{R_{\mathrm{H}}} = \frac{2(N-2)!}{N!} \sum_{i<j} \frac{1}{\|r_{ij}\|} \, , \tag{5}$$

where r_{ij} is the separation vector between the *i*th and *j*th galaxies and N is the total number of objects. The benefit of using a mean harmonic radius is that it more accurately measures the effective radius of the gravitational potential of the cluster members (Araya-Melo et al. 2009), important when considering the virial state of a system. This radius also has the benefit of being independent of the cluster centre allowing it to reflect internal structure of the system, putting extra weight on objects that are closer together (Araya-Melo et al. 2009). The virial radius for the entire system is related to the mean harmonic radius by $r_{\mathrm{vir}} \approx 2R_{\mathrm{H}} = 0.64$ Mpc (e.g. Girardi et al. 1998; Merchan & Zandivarez 2005).

Taking the values calculated for the velocity dispersions of each of the subclusters along with the harmonic radius for each, 68 per cent CI virial mass estimates are found to be $M_{\mathrm{vir}} = 6.0^{+1.3}_{-2.9} \times 10^{14}$ M$_\odot$ for A2146-A and $M_{\mathrm{vir}} = 2.5^{+3.0}_{-1.7} \times 10^{14}$ M$_\odot$ for A2146-B (we note here that subcluster B was found not to be well described by a Gaussian distribution), giving a mass ratio of 2.4. As an estimate for the total mass, we take the sum of the two estimates, since the assumption that the individual clusters are virialized is likely more appropriate than assuming that the system as a whole is virialized. This yields $M_{\mathrm{vir}} = 8.5^{+4.3}_{-4.7} \times 10^{14}$ M$_\odot$. Note that the error bars do

not reflect systematic errors which can change the mass estimate, even when the system is not in the throes of a merger; this simple dynamical estimate assumes a virialized spherical mass distribution with isotropic velocity dispersion.

The large errors in the mass estimates are due to the large errors inherent to the velocity dispersions. Since the virial mass is proportional to the square of the velocity dispersion, the error on the mass estimates is quite large. The 68 per cent CI level corresponds to a 1σ uncertainty. For a discussion of the impact of systematic and model-dependent errors on the mass estimates, see Section 6.

Since the estimates of mass from the kinematics of galaxies make several simplifying assumptions, we consider now an alternative estimate of the mass of each subcluster derived from a scaling relation between velocity dispersion and mass. Evrard et al. (2008) used N-body simulations to obtain a prediction for the relationship between mass and velocity dispersion of dark matter haloes. The advantage of this type of approach is that it includes more complex dynamical behaviour. Although their simulations were carried out using only dark matter, since galaxies and dark matter particles can both be treated as collisionless particles moving in a cluster potential, they are expected to have approximately the same velocity dispersion (Okamoto & Habe 1999; see also discussion in Evrard et al. 2008). Using the Evrard et al. (2008) relation

$$M_{200}E(z) = 9.358 \times 10^{14} \times (\sigma_v/1000)^{2.975} \, h^{-1} \, \mathrm{M_{\odot}} \,, \tag{6}$$

with the parameter $E(z) = 1.264$ at the cluster redshift and for the cosmology we work in, and determining the mass estimate for each cluster gives a total mass of $M_{200} = 2.0^{+2.0}_{-1.4} \times 10^{15} \, \mathrm{M_{\odot}}$.

The observed non-Gaussianity of A2146-B in conjunction with the system not being dynamically relaxed will contribute to an overestimation of the velocity dispersion for each subcluster component. The Evrard et al. (2008) scaling relation does not account for these and therefore it is likely that the mass will be overestimated as well.

Specifically for merging clusters, there have been studies using simulations to investigate the accuracy of various ways of estimating mass (Pinkney et al. 1996; Zuhone et al. 2009) or focusing on specific merger systems (e.g. Zuhone et al. 2009). For clusters with a mass ratio of 3:1, Pinkney et al. (1996) show that the mass inferred from a simple application of the virial theorem, and when subclustering is ignored in the analysis, can be biased by as high as a factor of 2. The maximum bias arises when the clusters are merging with an axis along the line of sight, and is somewhat less in mergers with an axis close to the plane of the sky, though still up to a factor of 1.5. The hydrodynamic simulations of Zuhone et al. (2009) are consistent with the earlier work of Pinkney et al. (1996). Zuhone et al. (2009) also support accounting for separate subclusters when determining mass estimates from the velocities of galaxies in a merger system.

5.2 Two-body dynamics

We undertake a dynamical analysis of the system using a two-body model, making the assumption that our system consists of two dominant subclusters, which is reasonable based on the projected density map (see Fig. 5). We use the methods adopted by Beers et al (Beers, Geller & Huchra 1982), to which the reader is referred for further details, and also follow the formalism presented in e.g. Girardi et al. (1998), Barrena et al. (2002) and Ferrari et al. (2005). Taking the total mass of the system derived from the virial mass estimates and the difference in radial velocities of the two subclusters, we calculated the angle between the merger axis and the plane of the sky, and the age of the merger. Note that this method assumes

point masses on radial orbits with no net rotation. The subcluster haloes will also most likely be overlapping in a recent merger. Making these assumptions in this analysis will add systematic and model-dependent uncertainties to the results obtained. Therefore the solutions will be approximations to the dynamics of A2146. The coupled equations, which describe the time evolution of the system, are closed by setting $t = t_0 = 3.4 \times 10^{17}$ s, the age of the Universe at the Abell 2146 system redshift $z = 0.2323$.

The parametric solutions to the equations of motion are given as follows:

$$R = \frac{R_{\mathrm{M}}}{2}(1 - \cos(\chi)) \,; \tag{7}$$

$$t = \left(\frac{R_{\mathrm{M}}^3}{8GM}\right)^{1/2}(\chi - \sin(\chi)) : \tag{8}$$

$$V = \left(\frac{2GM}{R_{\mathrm{M}}}\right)^{1/2}\frac{\sin(\chi)}{1 - \cos(\chi)} \,, \tag{9}$$

where R is the spatial separation, V is the relative velocity between the two BCGs, R_{M} is the separation of the two subclusters at maximum expansion, M is the total virial mass of the system, and χ is the so-called developmental angle.

The limits of the bound solutions can be found by considering the gravitational binding energy in the following relation

$$V_{\mathrm{R}}^2 R_{\mathrm{P}} \le 2 \, GM_{\mathrm{Total}} \sin^2(\alpha) \cos(\alpha), \tag{10}$$

where V_{R} is the difference in radial velocities of the two subclusters and R_{P} is the projected separation of the cores of the two subclusters.

Since the velocity distributions of the subclusters, A2146-A and A2146-B, do not precisely follow a Gaussian distribution, the difference in the mean radial velocity of the subclusters from a Gaussian fit (from Fig. 4) will not yield an accurate value of V_{R}. We therefore opt to use the difference in radial velocities of the two BCGs in each of the subclusters as a determination of V_{R}.

The spectra of the two BCGs are shown in Section 3 (Fig. 3). The BCG in A2146-B has a strong absorption spectrum with well-defined features, as is typical of BCGs. The spectrum of the BCG in A2146-A, however, shows many emission lines. The three most prominent features are H β and two [O III] lines. Zooming in on this spectrum (Fig. 7) shows the characteristic absorption spectrum expected for an elliptical galaxy with additional strong emission features.

While most of the absorption features are blended with emission features, making it difficult to accurately determine redshift, the Na D (rest wavelength of 5895 Å) feature is relatively unblended and yields a velocity of ~69 612 km s^{-1}. This is a lower redshift than determined through cross-correlation methods for the BCG which rely on the emission lines (69 897 km s^{-1}). Canning et al. (2012) show that much of the emission line gas in the A2146-A BCG is offset in a plume from the centre of the galaxy which may be the cause of the discrepancy in the radial velocities of the emission and absorption lines.

Calculating V_{R} as the difference between the absorption line spectrum of A2146-B and the emission spectrum of A2146-A gives a value of $V_{\mathrm{R}} = 850 \pm 60$ km s^{-1}. Using instead the Na D absorption feature yields a value of $V_{\mathrm{R}} = 620$ km s^{-1}. Nominally, it would be advantageous to take the velocities of the absorption lines of the galaxies, however, as the BCG in subcluster A is also offset from its predicted location – leading, rather than trailing, the cool core, which may indicate that the BCG is not in this case a good
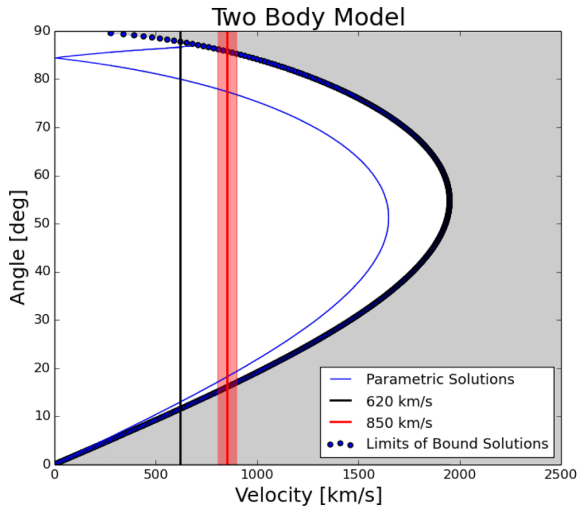
Figure 6. Projected angle from the plane of the sky, α, plotted against the difference in radial velocities of the subclusters, V_R. The black vertical line gives the solutions for $V_R = 620$ km s^{-1} and the red for $V_R = 850 \pm 60$ km s^{-1}. The red shaded area around V_R represents the errors in radial velocity from the cross-correlation. The dotted curve represents the limits of the bound solutions as calculated from equation (8). The grey region represents the area where only unbound solutions would exist. The intercept of the vertical lines gives solutions corresponding to $\alpha = 13°$–$19°$, $V = 2600$–2800 km s^{-1}, and $R = 0.70$–0.72 Mpc.

tracer of the centre of the mass distribution – we opt to consider the uncertainty as the relatively broad range in velocities from the emission and absorption spectra.

We therefore take V_R to be in the range 620 km s^{-1} to 850 $\pm$ 60 km s^{-1} in the two-body analysis. R_P is taken as the projected separation of the two BCGS. At the cluster redshift this corresponds to 0.69 Mpc.

The radial velocity and projected radius are related to the system parameters as follows:

$$V_R = V\sin(\alpha); R_P = R\cos(\alpha). \quad (11)$$

Solving equations (7), (8) and (9) iteratively yields the solutions shown in Fig. 6. Plotting V_R shows the solutions for our system. While there are solutions of α close to $80°$, the presence of the observed shocks in the X-ray analysis (Russell et al. 2010) and the estimated value of $17°$ (Canning et al. 2012), suggests that the merger is close to the plane of the sky. This allows us to take the range of solutions for $\alpha = 13°$–$19°$, which are very close to the values derived by Canning et al. (2012). The results from the two-body model analysis are $V = 2600$–2800 km s^{-1} for the relative velocity, and $R = 0.70$–0.72 Mpc for the separation. Assuming a collision site of $\approx R/2$, half way between the two subclusters, yields a merger age of 0.24–0.28 Gyr.

6 DISCUSSION

X-ray observations of Abell 2146 have revealed the system has two clear shock fronts and a gas structure similar to the Bullet cluster (Markevitch et al. 2002) showing it must be in the throes of a major merger. The detection of two clear shock fronts also indicate that the merger should be in an early stage. However, the Abell 2146 system presents a couple of challenges to that hypothesis.

The first is that the A2146-A subcluster BCG is located behind the bow shock and in the wake of the ram pressure stripped cool

core rather than leading it (see Russell et al. 2010 and Canning et al. 2012). As mentioned in Section 1 shortly after a galaxy cluster collision the intracluster medium is expected to lag behind the bulk of the mass distribution traced by the dark matter and the major concentrations of cluster galaxies (e.g. Clowe et al. 2006).

One possibility for the unusual location of the BCG could be that the cluster merger is not in its early stages (e.g. Hallman & Markevitch 2004). In the later stages of a galaxy cluster merger the collisionless matter distributions slow due to gravity allowing the gas to catch up and be accelerated in a 'gravitational slingshot' beyond the dominant mass distribution. Other possibilities are that the system may not be adequately represented by a two-body collision with the cluster containing complex substructure, or that the merger is somewhat off-axis.

Examining the redshifts of our target galaxies, we find 63 galaxies are likely members of the A2146 system. An analysis of the projected density peaks of the galaxies (see Section 4.2) shows that the Abell 2146 system is dominated by two subclusters. Our data do not provide evidence for other more complicated structures such as other merging groups or subclusters. We use the KMM algorithm to assign subcluster membership to the two subclusters and find 35 subcluster member galaxies in A2146-A and 28 in A2146-B. Application of the DS test to determine substructure was inconclusive. However, we emphasize that in Dressler & Shectman (1988) and in Pinkney et al. (1996), the sensitivity of the DS test to substructure in merger systems is shown to be diminished when the subclusters are of similar mass and when their merger axis is close to the plane of the sky, as is likely the case in Abell 2146.

Given that the system appears to be fairly well described by two dominant subclusters, we undertook a simple two-body analysis of the subcluster velocities and positions (Section 5.2 and Fig. 6) to determine the properties of the merger. As the velocity distributions of the subclusters are not both well described by Gaussian distributions, we choose to use the BCGs as a tracer of the centre of the subcluster mass distributions. We note here that in the case of subcluster A2146-A this may be incorrect since, as mentioned above, the BCG is offset from the expected location of the centre of the mass distribution; whilst the centroid of the distribution of red sequence galaxies is approximately coincident with the X-ray cool core, the BCG appears to lag behind the cool core. If a collision has offset the BCG, we may therefore expect the BCG velocity not to accurately trace the subcluster velocity centroid. The A2146-A BCG not only shows absorption features but also strong emission features in the spectrum which have a velocity offset of $\sim$230 km s^{-1}. This is significantly larger than the errors in the velocities from cross-correlation ($\sim$30 km s^{-1}). The centroid of the subcluster velocity distribution falls in between the emission and absorption values (A2146-A; BCG emission 69 897 km s^{-1}, BCG absorption 69 612 km s^{-1}, Centroid (KMM) 69 878 km s^{-1}: A2146-B; BCG absorption 68 827 km s^{-1}, Centroid (KMM) 69 710 km s^{-1}; WYFFOS spectra published in Canning et al. 2012 determined similar velocities of 69 753 and 68 940 km s^{-1}, from single Gaussian fits to the emission and absorption spectra, for BCG A and B, respectively). We therefore choose to use the full range of velocities from the absorption and emission lines in the A2146-A BCG in the two body analysis to allow a conservative estimate of the merger axis angle and time-scale.

Despite these uncertainties in cluster velocity centroid, the merger age, for bound solutions close to the plane of the sky, is still predicted to be young (0.24–0.28 Gyr), similar to that determined for the Bullet cluster (Barrena et al. 2002). The subclusters are therefore likely being observed shortly after first core passage. The unusual BCG

position is therefore unlikely to be due to a gravitational 'slingshot' of the gas past the galaxies (see e.g. Hallman & Markevitch 2004).

The merger axis is determined to be very close to the plane of the sky with $\alpha = 13°–19°$. The additional α solution (top of Fig. 6) that would correspond to a line-of-sight merger is unlikely due to Russell et al. (2010, 2012) observing both forward and reverse X-ray shock fronts. Observations of merger shocks are rare in X-ray observations as they are easily diluted by projection effects, they are therefore most prevalent in systems which are close to the plane of the sky. We therefore conclude that the unusual BCG location is not due to projection effects in a line-of-sight merger.

These findings for the merger time-scale and merger axis are also consistent with the presence of the two large shock fronts seen in *Chandra* X-ray observations (Russell et al. 2012), since later in the merger the shock fronts would not be visible, and for a larger angle with respect to the plane of the sky their sharp edges would be smeared by projection effects.

Although the two-body model is useful for estimating the dynamical history of merger systems, the assumptions that the clusters are point masses with constant mass over time, start to break down when they begin to merge. The analysis also does not include a change in relative velocity of the clusters with time. In the context of the Bullet cluster, Nusser (2008) discusses several limitations of the two-body model, for example how dynamical friction and tidal stripping are not included in this type of analysis. Both of these effects act to reduce the relative speeds of the cluster components. Although hydrodynamic simulations are the most accurate way to model the dynamics of merger systems, there are prohibitive in terms of the complexity of setting up the simulations, and the computational expense. Dawson (2013) presents a novel approach where the computational requirements fall somewhere between the two-body model and hydrodynamic simulations. By comparison with full hydrodynamic simulations of the Bullet cluster, this method is accurate to about 10 per cent in determining parameters describing the clusters and their merger trajectory. Required inputs to this dynamical modelling approach include spectroscopic redshifts for cluster members, arising from this work, and additional mass estimates available from the weak lensing analysis (King L. J., in preparation). Thus application of the Dawson (2013) method to Abell 2146 will be the topic of future work.

The second challenge for Abell 2146 is its apparent lack of radio emission, neither radio relics, which would be expected to be associated with the shock fronts, nor a radio halo have been seen (Russell et al. 2011). Large-scale diffuse radio emission in clusters has only been found in merging systems and as such it could be a useful diagnostic of the statistics of dynamically relaxed and merging systems. However, the mechanisms which form this diffuse radio emission and the conditions required for their formation are not yet known.

Diffuse radio emission on Mpc-scales in clusters requires local particle acceleration where either a pre-existing electron population is re-accelerated by merger turbulence (e.g. Brunetti et al. 2001; Petrosian 2001) or emitting electrons are continuously injected by collisions between cosmic ray protons and thermal protons (e.g. Dennison 1980; for reviews of extended radio emission in clusters see Feretti & Giovannini 2008; Ferrari et al. 2008; Feretti et al. 2012). The recent discovery of extremely steep radio halo spectra (e.g. Brunetti et al. 2009; Dallacasa et al. 2009) together with the non-detection of nearby clusters at γ-ray wavelengths (e.g. Ackerman et al. 2010; Brunetti et al. 2012) favours turbulent re-acceleration models over the 'secondary' continuous injection models.

Correlations between the synchrotron power in radio haloes, P_{radio}, and the galaxy cluster X-ray luminosity, L_X and temperature, T_X, have been found, which also show a bi-modailty for merging and non-merging galaxy clusters (e.g. Liang et al. 2000; Kemnper & Sarazin 2001; Bacchi et al. 2003; Cassano, Brunetti & Setti 2006; Brunetti et al. 2007). Clusters with detected radio haloes have P_{radio} correlated with L_X and show a disturbed morphology consistent with merging where there is no radio halo detected, and with only upper limits on radio luminosity, the clusters generally appear more relaxed and lie roughly an order of magnitude below this correlation (Brunetti et al. 2009; Rossetti et al. 2011). However, some clusters, such as Abell 2146, have been found which confound this bi-modality in the X-ray (e.g. Giovannini & Feretti 2000; Cassano et al. 2010; Russell et al. 2011).

Russell et al. (2011) showed the 3σ radio halo upper limit is a factor of ~5 times lower than predicted given its X-ray luminosity. X-ray luminosity is boosted in a merger and this factor is greater for young mergers (Ricker & Sarazin 2001) so the confirmed young age of the Abell 2146 system (being only 0.24–0.28 Gyr old) and the near equal masses of the subclusters indicates its X-ray luminosity is likely to be enhanced by a factor of ~2–5. A boost this significant could place Abell 2146 back on the relation for merging clusters. However, the age since core passage is similar to other systems in which radio haloes have been detected.

Brunetti et al. (2012) examine a sample of radio halo clusters from the GMRT Radio Halo Survey and find that cluster synchrotron emission is suppressed on time-scales of only a few hundred Myr. The simulations of Donnert et al. (2013), albeit for a 1:7 mass ratio merger, suggest that the radio halo luminosity should be increasing rapidly during infall and through core passage, with the X-ray and radio luminosity, within a few hundred Myr, being boosted by factors of 2 and 30, respectively. They find the radio emission starts to decay roughly 0.5 Gyr after core passage. While time-scale may be relevant in boosting the X-ray luminosity and therefore in where Abell 2146 should sit on the $P_{radio}–L_X$ relation, these and other simulations suggest that the time-scale since core passage for Abell 2146 is not too short or too long for the generation of a radio halo.

Cluster mass is thought to be a key component of radio halo generation in galaxy clusters (Cassano & Brunetti 2005). Basu (2012) examine the radio–SZ correlation for clusters on the basis that the integrated SZ signal is a more robust indicator of the cluster mass regardless of dynamical state than the X-ray luminosity (e.g. Motl et al. 2005; Nagai, Kravtsov & Vikhlinin 2007). A correlation is found for the radio power and integrated SZ signal, Y_{SZ} for the sample of clusters and no bi-modality is detected between those clusters which are relaxed and those which are disturbed. The authors suggest the bi-modality with X-ray properties may be due to a bias in the radio quiet, X-ray selected clusters, being selected towards lower mass cool core clusters. However, they note that their sample size for radio quiet systems is small and so a weaker bi-modality might still exist. Cassano et al. (2013) find the converse, that a bi-modailty exists, in both the $P_{radio}–L_X$ and $P_{radio}–Y_{SZ}$ relations with all relaxed systems having radio halo upper limits which sit $>2\sigma$ below the relation. However, they suggest mass is also important and that the bi-modality only exists for 'SZ-luminous' $Y_{SZ} > 6 \times 10^{-5}$ Mpc^2, or alternatively massive, $M_{500} > 5.5 \times 10^{14}$ M$_\odot$ galaxy clusters.

The scaling relation of Evrard et al. (2008), while robust, does not account for the observed subclustering or dynamical state of Abell 2146. While our individual subcluster masses similarly suffer from the dynamics of the merger the total mass as the sum of the subcluster masses rather than assuming one virialized system should

Table 1. Summary of mass estimates for Abell 2146. All masses are in units of $M_\odot$.

Mass	M_{500}	M_{200}
Dynamics	$5.4^{+2.7}_{-3.0} \times 10^{14}$	$8.5^{+4.3}_{-4.7} \times 10^{14}$
SZ	$4.3^{+0.6}_{-0.6} \times 10^{14}$	$5.6^{+0.7}_{-0.7} \times 10^{14}$
X-ray	$\approx 7^{+2}_{-2} \times 10^{14}$	–

yield value more in line with previous estimates. We therefore use a total mass of $M_{vir} = 8.5^{+4.3}_{-4.7} \times 10^{14}$ M$_\odot$ giving a mass ratio of approximately 2.4:1 (A2146-A to A2146-B). The large uncertainties in the mass estimates preclude determining which subcluster is in fact the more massive component with a high degree of confidence. However, the system appears to have undergone a recent relatively equal-mass merger. The X-ray analysis found that the bow shock and upstream shock are of comparable strength, which is consistent with a close to equal mass merger, however a 1:4 mass ratio with A2146-B being more massive than A2146-A was favoured Russell et al. (2010). For higher mass ratio systems, such as the Bullet cluster (Clowe et al. 2006) with a ratio of $\approx$10:1, the perturbation to the gravitational potential of the merger is much smaller and therefore will produce a much weaker upstream shock. Our dynamical mass ratio estimate is consistent with a weak lensing analysis of the system (King L. J., in preparation).

The NFW (Navarro, Frenk & White 1996) r_{200} value of the system is approximately equal to the virial radius, or to twice the harmonic radius calculated in Section 5.1, yielding a value of $r_{200} = 0.64$ Mpc. Assuming an NFW mass profile and a halo concentration of 4 typical of massive galaxy clusters (see collation from King & Mead 2011), an estimate of $r_{500} \approx 0.42$ Mpc was calculated, corresponding to $M_{500} = 5.4^{+2.7}_{-3.0} \times 10^{14}$ M$_\odot$.

To take into account the overestimate in mass due to the system having undergone a recent merger, a surface pressure term (SPT) can be subtracted from the viral mass to get a more accurate estimate of the true mass of the system (The & White 1986). Assuming the velocities are isotropic, the SPT correction can be taken as SPT $= 0.2 \times M_{vir}$ (Girardi et al. 1998). The reduction of the mass due to the SPT correction would result in a lower mass estimate of $M_{200} = 6.8 \times 10^{14}$ M$_\odot$ and $M_{500} = 4.3 \times 10^{14}$ M$_\odot$.

For Abell 2146, SZ observations (Rodríguez-Gonzálvez et al. 2011) yielded a total system mass inside r_{200} of $M_{200,SZ} = 4.1 \pm 0.5 \times 10^{14} h^{-1}$ M$_\odot$ (or $5.6^{+0.7}_{-0.7} \times 10^{14}$ M$_\odot$ using the same cosmology as this paper, i.e. $h = H_0/70$ km s^{-1}Mpc^{-1}). This is a factor of ~1.5 smaller than our dynamical virial mass estimate for the total system mass not including an SPT correction, or roughly 1.2 times smaller with the SPT correction, bringing the calculated M_{200} within the errors of the SZ mass estimate. The M_{500} and M_{200} values calculated from the SZ (taking $h = H_0/70$ km s^{-1}Mpc^{-1}), our dynamics analysis, and the X-ray analysis of Russell et al. (2012) are compiled in Table 1.

When correcting M_{500} for the SPT, and using the direct scaling of $M_{500} - P_{1.4}$, shown in Fig. 7 (fig. 3 from Cassano et al. 2013), we find an expected radio halo power of $P_{1.4} \approx 4 \times 10^{23}$ Watt Hz^{-1}, marked with the dashed black horizontal line in Fig. 7. The solid purple horizontal line marks the calculated 3σ upper limit for A2146 from the GMRT radio observations by Russell et al. (2011). This observational upper limit is therefore very similar to the radio power predicted by the observed $M_{500} - P_{1.4}$ correlation for merging systems, using a dynamical mass estimate.

A lower M_{500} value could be the leading factor as to why no extended radio emission is detected, and this is accommodated within the errors on the dynamical mass, particularly if we include the
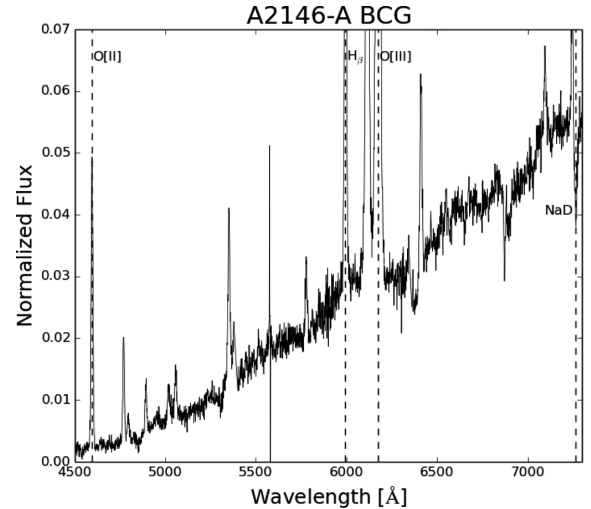

Figure 7. Zoomed in view of the spectrum for the BCG in A2146-A. Both absorption and emission features are clearly visible and the radial velocity of the emission features are offset by $\approx$+230 km s^{-1} from the BCG. Both absorption and emission features are labelled.

SPT. As the radio observing sensitivity increases in the future, faint extended radio emission may well be detected and the possibility of a mass threshold for radio haloes in merging clusters will be clarified. Furthermore, the prospects for assessing the dependence of radio halo production on other factors will improve with studies of large samples of major cluster mergers.

7 CONCLUSIONS

We present a dynamical analysis of the galaxy cluster merger system Abell 2146 using multi-object spectroscopic observations from the Gemini North Telescope. We employ substructure tests such as the DS test (Dressler & Shectman 1988), analysis of an adaptive kernel density map (Pisani 1993), and application of the KMM algorithm (Ashman et al. 1994) using the position information of the galaxies to conclude that the system is dominated by two main substructures, and is likely well described by a two-body collision. One cluster is located in the south-east (A2146-A) and the other in the north-west (A2146-B). An average redshift of $z = 0.2323$ was calculated with velocity dispersions of 1130^{+120}_{-320} km s^{-1} and 760^{+360}_{-340} km s^{-1}, respectively, for the A2146-A and A2146-B subclusters. The main results are as follows.

(i) From the 63 spectroscopically confirmed A2146 system members, we estimate a total virial mass of $M_{vir} = 8.5^{+4.3}_{-4.7} \times 10^{14}$ M$_\odot$, without any correction applied for the ~20 per cent boost in mass due to the system having undergone a recent merger (e.g. The & White 1986).

(ii) The two subclusters have a close to 2.4:1 mass ratio indicating that this is a major merger.

(iii) A two-body analysis of the system yielded an angle between the merger axis and plane of sky of approximately $13°–19°$ and a time since core passage of the merger of approximately 0.24–0.28 Gyr.

These findings for the dynamics are consistent with the observation of large shock fronts on *Chandra* X-ray images (Russell et al. 2010; 2012). We conclude from our analysis that the unusual location of the BCG, behind, not in front of the shock front and X-ray cool core, is not due to the merger being in a late stage of its

evolution with the gas experiencing a gravitational slingshot beyond the main mass distribution.

Despite the lack of an observed radio halo, simulations of our calculated time-scale and near equal mass ratio of the merger would seem to favour the generation of a radio halo (e.g. Brunetti et al. 2012; Donnert et al. 2013). However, the final mass of the system, and therefore necessarily the progenitor masses of the two subclusters, is fairly low, compared with other similar cluster mergers. Cassano et al. (2013) suggest that a bi-modality in radio halo properties for merging and non-merging systems may require a total mass threshold of about $M_{500} > 5.5 \times 10^{14}$ M$_\odot$. Uncertainties on the mass estimates are very large, however, Abell 2146 would lie close to this threshold. Deeper radio data on this and other merging systems that appear to lack radio haloes would be critical for testing whether a threshold in mass exists. Magnetohydrodynamic simulations of the system, constrained by the wealth of observational data, will further our understanding of the distribution of luminous and dark matter in the system, as well as the radio emission. For the Bullet cluster, recent work by Lage & Farrar (2014) illustrates that this approach provides much insight into merger systems. Application of the Dawson (2013) method for dynamical modelling will provide a more accurate description of the geometry of the merger than provided by the two-body model, also greatly narrowing down the parameter space for MHD simulations.

Conflicting scenarios have been proposed where merger events may be a catalyst to spur star formation – for example shock fronts moving through the ICM and triggering further starbursts (Mihos & Hernquist 1996; Bekki & Couch 2003) – or to quench star formation via ram-pressure stripping (Fujita et al. 1999). Detailed analysis of the [O II], [O III], H α, and H β spectral lines is currently underway (Lee et al. in preparation), in order to estimate the star formation rates in the cluster galaxies as discussed in Ferrari et al. (2005).
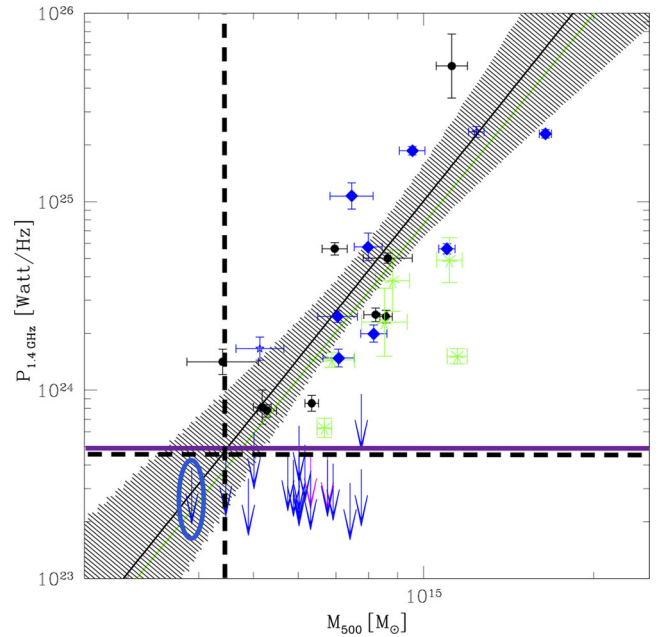
ACKNOWLEDGEMENTS

Figure 8. Distribution of clusters in the $P_{1.4} - M_{500}$ diagram (fig. 3 from Cassano et al. 2013). The blue circles were changed to diamonds for clarity and additional lines are added corresponding to dynamical and X-ray analysis. The various different symbols indicate haloes belonging to the extended Giant Metrewave Radio Telescope (GMRT) Radio Halo Survey (Cassano et al. 2013), or EGRHS, (blue diamonds); haloes from the literature (black circles); haloes with very steep spectra (USSRH, green asterisks); A1995 and Bullet cluster (blue stars); cool core clusters belonging to the EGRHS (magenta arrows). Best-fitting relations to giant RHs only (black lines) and to all RHs (including USSRH, green dashed lines) are reported. The circled blue arrow is A2146 with an M_{500} and $P_{1.4}$ reported by Cassano et al. (2013). The dashed line shows A2146 and its derived M_{500} from dynamical analysis. This corresponds to a radio halo power upper limit of $P_{1.4} \approx 4 \times 10^{23}$ W Hz^{-1} for a mass of $M_{500} = 4.3 \times 10^{14}$ M$_\odot$. The horizontal purple line marks the calculated 3σ upper limit for Abell 2146 from Russell et al. (2011).

REFERENCES

Ackerman M., Ajello M., Allafort A., Baldini L., Ballet J., Barbiellini G., Bastieri D., 2010, ApJ, 717, L71
Araya-Melo P. A., Van De Weygaert R., Jones B. J., 2009, MNRAS, 400, 1317
Ashman K. M., Bird C. M., Zepf S. E., 1994, AJ, 108, 2348
Bacchi M., Feretti L., Giovannini G., Govoni F., 2003, A&A 400, 465
Barrena R., Biviano A., Ramella M., Falco E. E., Sietz S., 2002, A&A, 386, 861
Basu K., 2012, MNRAS, 421, L112
Beers T. C., Geller M. J., Huchra J. P., 1982, ApJ, 257, 23
Beers T. C., Flynn K., Gebhardt K., 1990, AJ, 100, 32
Bekki K., Couch W. J., 2003, ApJ, 596, 13
Bertin E., Arnouts S., 1996, A&AS, 117, 393
Brunetti G., Setti G., Feretti L., Giovannini G., 2001, MNRAS, 320, 365
Brunetti G., Venturi T., Dallacasa D., Cassano R., Dolag K., Setti G., 2007, ApJ, 670, L5

Brunetti G., Cassano R., Dolag K., Setti G., 2009, A&A, 507, 661

Brunetti G., Blasi P., Reimer O., Rudnick L., Bonafede A., Brown S., 2012, MNRAS, 426, 956

Buote D. A., 2001, ApJ, 553, L15

Canning R. E. A. et al., 2012, MNRAS, 420, 320

Cassano R., Brunetti G., 2005, MNRAS, 357, 1313

Cassano R., Brunetti G., Setti G., 2006, MNRAS, 369, 1577

Cassano R., Ettori S., Giacintucci S., Brunetti G., Markevitch M., Venturi T., Gitti M., 2010, ApJ, 721, L82

Cassano R. et al., 2013, ApJ, 777, 141

Clowe D., BradacŽ M., Gonzalez A. H., Markevitch M., Randall S. W., Jones C., Zaritsky D., 2006, ApJ, 648, L109

Dallacasa D. et al., 2009, ApJ, 699, 1288

Dawson W. A., 2013, ApJ, 772, 131

Denison B., 1980, ApJ, 239, L93

Donnert J., Dolag K., Brunetti G., Cassano R., 2013, MNRAS, 429, 3564

Dressler A., Shectman S., 1988, AJ, 95, 985

Evrard A. E. et al., 2008, ApJ, 672, 122

Feretti L., Giovannini G., 2008, in Plionis M., Lopez-Cruz O., Hughes D., eds, Lecture Notes in Physics, Vol. 740, A Pan-Chromatic View of Clusters of Galaxies and the Large-Scale Structure. Springer, Dordrecht, p. 143

Feretti L., Giovannini G., Govoni F., Murgia M., 2012, A&AR, 20, 1

Ferrari C., Benoist C., Maurogordato S., Cappi A., Slezak E., 2005, A&A, 430, 19

Ferrari C., Govoni F., Schindler S., Bykov A. M., 2008, Clusters of Galaxies. Springer, New York, p. 93

Fujita Y., Takizawa M., Nagashima M., Enoki M., 1999, PASJ, 51, 1

Gallazzi A., Brinchmann J., Charlot S., White S., 2008, MNRAS, 383, 1439

Giovannini G., Feretti L., 2000, New Astron., 5, 335

Girardi M., Giuricin G., Mardirossian F., Mezzetti M., Boschin W., 1998, ApJ, 505, 74

Hallman E. J., Markevitch M., 2004, ApJ, 610, L81

Kempner J. C., Sarazin C. L., 2001, ApJ, 548, 639

King L. J., Mead J. M., 2011, MNRAS, 416, 2539

Kurtz M. J., Mink D. J., 1998, PASP, 110, 934

Lage C., Farrar G., 2014, ApJ, 787, 144

Liang H., Hunstead R. W., Birkinshaw M., Andreani P., 2000, ApJ, 544, 686

Markevitch M., Vikhlinin A., 2001, ApJ, 563, 95

Markevitch M., Vikhlinin A., 2007, Phys. Rep., 443, 1

Markevitch M., Gonzalez A. H., David L., Vikhlinin A., Murray S., Forman W., Jones C., Tucker W., 2002, ApJ, 567, L27

Markevitch M., Gonzalez A. H., Clowe D., Vikhlinin A., Murray S., Forman W., Jones C., Tucker W., 2004, ApJ, 606, 819

Merchan M. E., Zandivarez A., 2005, ApJ, 630, 759

Mihos J. C., Hernquist L., 1996, ApJ, 464, 641

Milosavljević M., Koda J., Nagai D., Nakar E., Shapiro P. R., 2007, ApJ, 661, L131

Motl P. M., Hallman E. J., Burns J. O., Norman M. L., 2005, ApJ, 623, L63

Nagai D., Kravtsov A. V., Vikhlinin A., 2007, ApJ, 668, 1

Navarro J. F., Frenk C. S., White S. D. M., 1996, ApJ, 462, 563

Nusser A., 2008, MNRAS 384, 343

Okamoto T., Habe A., 1999, APJ, 516, 591

Petrosian V., 2001, ApJ, 557, 560

Pinkney J., Roettiger K., Burns J. O., Bird C. M., 1996, ApJ, 104, 1

Pisani A., 1993, MNRAS, 265, 706

Randall S. W., Markevitch M., Clowe D., Gonzalez A. H., Bradac M., 2008, ApJ, 679, 1173

Ricker P. M., Sarazin C. L., 2001, ApJ, 561, 621

Rodríguez-Gonzálvez C., Olamaie M., Davies M. L., Fabian A. C., Feroz F., Franzen T. M., Zwart J. T., 2011, MNRAS, 414, 3751

Rossetti M., Eckert D., Cavalleri B. M., Molendi S., Gastaldello F., Ghizzardi S., 2011, A&A, 532, 123

Russell H. R., Sanders J. S., Fabian A. C., Baum S. A., Donahue M., Edge A. C., McNamara N. R., O'Dea C. P., 2010, MNRAS, 406, 1721

Russell H. R. et al., 2011, MNRAS, 417, L1

Russell H. R. et al., 2012, MNRAS, 423, 236

Sarazin C., 2001, in Feretti L., Gioia I. M., Giovannini G., eds, Astrophysics and Space Science Library, Vol. 272, Merging Processes in Galaxy Clusters. Kluwer, Dordrecht, p. 253

Springel V., Farrar G. R., 2007, MNRAS, 380, 911

Stuble M. F., Rood H. J., 1999, ApJ, 125, 35

The L. S., White S. D. M., 1986, AJ, 92, 1248

Waters C. Z., Zepf S. E., Lauer T. R., Baltz E. A., 2009, ApJ, 693, 46

ZuHone J. A., Ricker P. M., Lamb D. Q., Karen Yang H.-Y., 2009, ApJ, 699, 1004

APPENDIX

Table A1. Data for 63 spectroscopically confirmed cluster member galaxies in the field of Abell 2146. The radial velocities are calculated from RVSAO cross-correlation methods applied to our Gemini GMOS spectroscopic observations (PI Canning).

ID	RA (deg)	Dec (deg)	cz (km s^{-1})	Δcz (km s^{-1})	Subcluster (A/B)	Type (Emission/Absorption)
5	238.9647	66.372 98	694 84	24	B	Ab
13	238.9836	66.366 37	680 14	130	B	Ab
14	238.9839	66.376 59	691 28	47	B	Ab
16	238.9883	66.389 78	674 82	35	B	Ab
21	238.9973	66.372 49	701 86	16	B	Ab
22	238.9987	66.369 88	677 05	10	B	Em
23	239.0007	66.373 29	688 49	24	B (BCG)	Ab
24	239.0027	66.369 94	711 23	37	B	Ab
35	239.0064	66.366 87	685 17	17	B	Ab
36	239.0085	66.3711	711 63	31	B	Ab
39	239.013	66.3703	713 25	21	B	Ab
43	239.0155	66.379 42	683 98	19	B	Ab
47	239.0175	66.377	706 49	20	B	Ab
48	239.0196	66.356 06	704 06	31	B	Ab
50	239.022	66.3901	691 95	58	B	Ab
54	239.0246	66.367 91	719 30	49	B	Ab
55	239.025	66.3782	688 02	21	B	Em
57	239.0291	66.368 15	718 35	37	B	Ab
60	239.031	66.3541	705 04	78	A	Ab
61	239.034	66.349	692 49	78	A	Ab
63	239.034	66.3764	694 32	32	B	Ab
67	239.0385	66.3488	716 34	14	A	Ab
68	239.0385	66.3294	682 42	33	A	Ab
71	239.0403	66.360 81	728 76	16	A	Ab
76	239.0445	66.3462	710 54	81	A	Em
79	239.0495	66.361 06	699 24	27	A	Ab
80	239.0505	66.3496	713 65	25	A	Ab
81	239.0505	66.3534	693 71	43	A	Ab
83	239.052	66.3567	723 27	41	A	Em
87	239.0535	66.3701	699 25	38	A	Ab
90	239.056	66.333 81	683 68	54	A	Ab
92	239.0565	66.3565	678 10	37	A	Ab
94	239.058	66.3482	698 97	26	A (BCG)	Em
96	239.0601	66.344 56	700 33	22	A	Ab
105	239.067	66.3461	694 97	24	A	Ab
108	239.0691	66.342 59	680 75	21	A	Ab
109	239.0694	66.340 06	710 13	52	A	Ab
110	239.07	66.3467	689 29	16	A	Ab
113	239.0762	66.3713	687 90	28	A	Ab
115	239.0768	66.361 12	695 52	31	A	Ab
116	239.0795	66.3415	716 10	18	A	Ab
117	239.0799	66.340 54	690 59	32	A	Ab
120	239.0827	66.344 73	691 21	39	A	Ab
122	239.0835	66.3427	724 89	42	A	Em
123	239.0835	66.3564	716 83	35	A	Ab
128	239.0955	66.3482	706 73	31	A	Ab
135	239.1241	66.355 26	683 52	18	A	Ab
138	238.989	66.3766	686 24	30	B	Ab
139	239.0091	66.363 26	689 60	22	B	Ab
142	238.9803	66.363 38	693 23	23	B	Ab
143	238.9758	66.363 88	666 69	25	B	Ab
147	239.0616	66.338 45	698 60	14	A	Ab
149	239.0802	66.336 84	679 65	25	A	Ab
150	239.085	66.343	703 21	16	A	Ab
152	239.0406	66.345 49	676 38	18	A	Ab
153	239.058	66.356	700 31	22	A	Ab
154	239.04	66.3502	702 82	17	A	Ab
156	239.0025	66.3748	691 79	27	B	Ab
157	239.016	66.3708	689 56	27	B	Ab
164	239.0625	66.3677	711 60	39	A	Em
165	239.0184	66.364 44	690 28	31	B	Ab
168	239.0051	66.390 83	704 13	35	B	Em
170	238.959	66.3771	692 39	23	B	Ab

This paper has been typeset from a TEX/LATEX file prepared by the author.